INTERNATIONAL JOURNAL OF HYDROGEN ENERGY 40 (2015) 7335–7347

Available online at www.sciencedirect.com

ScienceDirect

journal homepage: www.elsevier.com/locate/he

Effect of structural defects on the hydriding kinetics of nanocrystalline Pd thin films

Renaud Delmelle [a,*], *Behnam Amin-Ahmadi* [b], *Marc Sinnaeve* [c], *Hosni Idrissi* [b,c], *Thomas Pardoen* [c], *Dominique Schryvers* [b], *Joris Proost* [c]

[a] *Laboratory for Advanced Analytical Technologies, Swiss Federal Laboratories for Materials Science and Technology, Überlandstrasse 129, CH-8600 Dübendorf, Switzerland*

[b] *Electron Microscopy for Materials Science, Department of Physics, University of Antwerp, Groenenborgerlaan 171, B-2020 Antwerp, Belgium*

[c] *Institute of Mechanics, Materials and Civil Engineering, Université catholique de Louvain, Place Sainte-Barbe 2, B-1348 Louvain-la-Neuve, Belgium*

ARTICLE INFO

Article history:
Received 14 November 2014
Received in revised form
21 February 2015
Accepted 3 April 2015
Available online 30 April 2015

Keywords:
Hydriding
Pd-H
Kinetics
Microstructure
Internal stress

ABSTRACT

While the microstructure of a metal is well-known to affect its equilibrium hydrogen uptake and therefore the hydriding thermodynamics, microstructural effects on the hydriding kinetics are much less documented. Moreover, for thin film systems, such microstructural effects are difficult to separate from the internal stress effect, since most defects generate internal stresses. Such a decoupling has been achieved in this paper for nanocrystalline Pd thin film model systems through the use of a high-resolution, in-situ curvature measurement set-up during Pd deposition, annealing and hydriding. This set-up allowed producing Pd thin films with similar internal stress levels but significantly different microstructures. This was evidenced from detailed defect statistics obtained by transmission electron microscopy, which showed that the densities of grain boundaries, dislocations and twin boundaries have all been lowered by annealing. The same set-up was then used to study the hydriding equilibrium and kinetic behaviour of the resulting films at room temperature. A full quantitative analysis of their hydriding cycles showed that the rate constants of both the adsorption- and absorption-limited kinetic regimes were strongly affected by microstructure. Defect engineering was thereby shown to increase the rate constants for hydrogen adsorption and absorption in Pd by a factor 40 and 30, respectively.

Introduction

Microstructure plays a crucial role in the mechano-chemical properties of materials, including their hydriding properties. In particular, the microstructure of a metal can offer several types of hydrogen trapping sites [1], in the bulk as well as on the surface and within subsurface layers. In the case of nanostructured thin films, the contribution of nonbulk-like

* *Corresponding author*. Tel.: +41 58 765 65 41; fax: +41 58 765 69 22.
E-mail address: renaud.delmelle@empa.ch (R. Delmelle).

http://dx.doi.org/10.1016/j.ijhydene.2015.04.017

effects to the total hydrogen content becomes significant, which makes thin films an attractive model system to study the impact of microstructural aspects on hydriding.

For instance, the grain size of nanocrystalline thin films is orders of magnitude smaller compared to bulk specimens. The resulting high density of grain boundaries with their disordered nature offers a high concentration of low-energy trapping sites for absorbed hydrogen atoms [2]. Using nanocrystalline Pd as a model system, Mütschele and Kirchheim described the energy distribution of these sites as Gaussian, with a width of 15 kJ/mol [3,4]. In addition to a very small fraction of lattice sites, the low-energy sites are occupied at low hydrogen concentrations, which increases the lower limit of the miscibility gap. But at high hydrogen concentrations, only the regular lattice sites can be additionally filled with hydrogen. Since the density of lattice sites is lower than in a bulk material, the mean hydrogen concentration is also lowered, which decreases the upper limit of the miscibility gap. Therefore, grain boundaries have a narrowing effect on the miscibility gap of metal-hydrogen systems. This particular distribution of trapping sites in the grain boundaries also affects the hydriding kinetics of metals. At very low hydrogen concentrations, grain boundary diffusion of hydrogen is virtually stopped by the deepest potential wells [5]. At high hydrogen concentrations, the opposite trend is observed, and the diffusion in the nanocrystalline material is faster than in bulk Pd [6–8].

Dislocations also play an important role in the hydriding of metals, as the compressive hydrostatic stress component induced by hydriding strongly interacts with the local tensile stress fields that the dislocations produce [1,9]. Dislocations in thin films can be generated by the deposition process, but they can also be created by both hydrogen absorption and desorption [1], where they accommodate the lattice mismatch associated to the hydride phase nucleation and growth in the solid solution. In particular, edge dislocations interact strongly with hydrogen atoms, with a binding energy of approximately 60 kJ/mol with the dislocation core [9]. This value is higher than the binding energy of hydrogen in regular Pd lattice sites [10]. The hydrogen enrichment region at the core of an edge dislocation can be imagined as a cylindrical surface of constant hydrostatic stress located below the dislocation glide plane [11–13]. As opposed to edge dislocations, the shear stress component generated by screw dislocations interacts poorly with the hydrostatic stress component of the interstitial hydrogen atoms [1]. It is also well-known that dislocations act as preferential pathways for hydrogen transport [14,15], thereby also affecting the hydriding kinetics.

Vacancies, another potential hydrogen trapping site [16], can also be expected to be present in high concentrations in room temperature deposited metallic films. Similarly to the hydrogen interaction with the surface, these open volume defects offer low-energy sites in which the hydrogen atoms form so-called vacancy complexes whose exact composition and stability are still under debate even for the Pd–H model system [17–19]. The hydriding kinetics of metals is usually reported to be enhanced by the presence of vacancies [20–22]. Precipitates can also act as hydrogen trapping sites [23], but they will not be considered in this work, which focuses on pure palladium.

The exact role of twins on hydrogen absorption in metals is as yet still unclear. Several authors claim that twins can act as hydrogen traps in a variety of steel alloys [24,25], while Danaie et al. concluded that twins do not modify the thermodynamic behaviour of hydrogen in magnesium [26]. One can expect that twins can act as traps only if the enthalpy of hydriding in regular lattice sites is high enough, which is not the case for all metals. On the other hand, Danaie et al. did observe a significant enhancement in the hydriding kinetics of their Mg powders. Twins can therefore also be considered as preferential pathways for hydriding. In this respect, Amin-Ahmadi et al. have recently shown that nanoscale Σ3 {111} coherent growth twin boundaries lose their coherency after hydriding in Pd thin films [27], which may suggest a strong interaction with hydrogen, similarly to grain boundaries.

The above studies provide clear evidence that microstructure constituents affect the equilibrium hydriding behaviour of metallic compounds. On the other hand, systematic, quantitative experimental studies on the effect of microstructure on the hydriding kinetics of different metals and alloys are still missing. As opposed to our previous study [28], whose objective was to study quantitatively the effect of internal stress on the hydriding kinetics of pure Pd thin films at constant microstructure, this paper is dedicated to the quantitative study of the effect of microstructure on the hydriding kinetics at constant internal stress. The choice of the Pd–H system was straightforward, since the latter earned its "model system" status in the course of the last century, notably because of its ability to readily absorb and release hydrogen at room temperature [29,30].

In this study, the microstructure of Pd films has been modified through a thermal annealing step in order to eliminate part of the defects that are generated by room temperature magnetron sputtering. The annealing process itself has been monitored in real time with high resolution in-situ curvature measurements, both in order to compare the hydriding properties of the annealed films with as-deposited specimens exhibiting the same initial internal stress state, and to correlate the stress evolution with defect recovery. Many authors indeed identified direct relationships between the stress evolution during annealing and the density of grain boundaries [31,32], point defects [33,34] and dislocations [31,34,35]. The twin concentration can also be expected to be affected by annealing [36,37], but should not give rise to volume changes, and hence to stress changes, although it is expected to affect the hydriding behaviour. The annealing process will be presented in detail first, followed by the study of the equilibrium hydriding behaviour of the Pd films using the same in-situ curvature measurement approach. The hydriding kinetics of the films will then be studied in quantitative detail, including the determination of the rate-limiting steps and the identification of possible microstructural effects on the rate constants for both hydrogen adsorption and absorption. Finally, defect statistics obtained by Transmission Electron Microscopy (TEM) will be compared with the internal stress data obtained during annealing and hydriding, in order to identify the exact nature of the defects responsible for the microstructural effect on the hydriding kinetics.

Experimental methods

For the purpose of this study, the experimental setup previously developed for high resolution in-situ monitoring of thin film hydride formation at room temperature [38] has been modified in order to allow for high temperature measurements in vacuum. This new setup is schematically shown in Fig. 1. The vacuum chamber is a T-shaped quartz tube connected to a pumping system from Vacotec SA, consisting of a primary rotary pump and a turbo molecular pump. Base pressures on the order of 10^{-6} mbar can be reached in the tube in about 20 min. Ar/H_2 gas mixtures (Alphagaz from Air Liquide, 1% H_2 in this work) can be introduced into the tube in order to impose a desired pressure, the latter being measured by two gauges (Alcatel ACC 2009 and ASD 2001).

The furnace, acquired from H & C SPRL, has been specifically designed for this setup. It has the shape of an octogonal right prism, and its eight resistances are circularly displayed around the center of its bases, where two circular holes allow introducing the quartz tube. A third circular hole allows the third extremity of the tube to be inserted in the upper part of the ceramic shield of the furnace, so that the laser beams only travel through vacuum and room temperature air. An insulating foam is used to prevent the heat from escaping from the space left by these 3 holes. Moreover, a continuous room temperature air flux is imposed above the quartz tube optical window when the furnace is running. Heating is possible up to 1000 °C, and specific temperature profiles can be programmed.

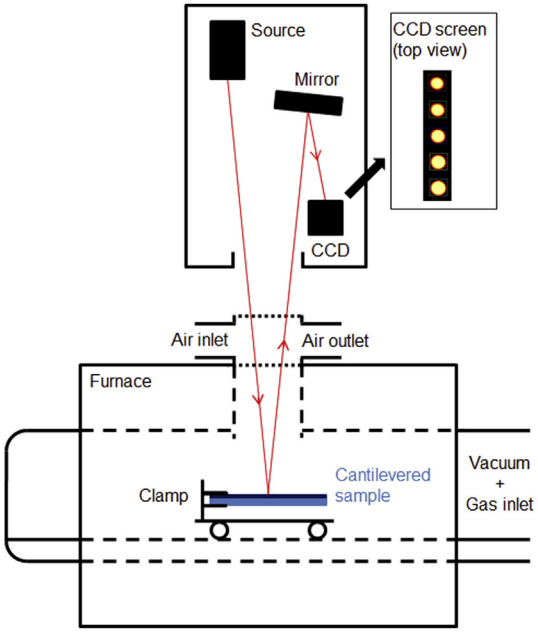

Fig. 1 – Schematic representation of the experimental setup used in this study for both annealing and hydriding. The red lines represent the trajectory of the laser beams used for in-situ curvature measurements. A top view of the CCD screen is also provided, showing the reflected laser spots. (For interpretation of the references to colour in this figure legend, the reader is referred to the web version of this article.)

A thermocouple has been installed in the middle of the tube in order to be able to measure the specimen temperature in real time. The clamping of the cantilevered specimens has been adapted to the high temperature conditions to which it can be exposed by using only quartz elements. The tube remained under high vacuum, on the order of 10^{-6} mbar, during the annealing cycles.

In the setup described above, the annealing and hydriding of the specimens can be monitored in-situ in the tube without vacuum break, i.e. thanks to the high resolution curvature measurement setup schematically represented in Fig. 1. It enables measurement of curvature with relatively high dynamic and time resolutions compared to similar laser-based curvature/deflection measurement techniques [39]. Van Overmeere et al [39] can be consulted for more details about this optical technique, whereas Ref. [38] details its application to thin film hydriding. In short, the measured change in specimen curvature – corresponding, in our case, to a consequence of the restricted volume change of a thin film attached to its substrate during annealing or hydriding – can be linked to the change of internal stress in the film thanks to the following relationship [40]:

$$\Delta\sigma = \frac{1}{6}\frac{E_S}{1-\nu_S}\frac{t_S^2}{t_f}\Delta\kappa, \quad (1)$$

where E_S and ν_S are the Young's modulus and Poisson ratio of the substrate, while t_S and t_f are their respective thicknesses.

Si wafers with 180 μm thickness were successively oxidized and coated with a 10 nm Ti adhesion film and a 150 nm Pd film. Cantilever specimens with dimensions 3×0.5 cm^2 were then cut from these wafers for the annealing and hydriding experiments. DC magnetron sputtering has been used to deposit the Ti and Pd films, with real-time monitoring of the specimen curvature as detailed in a previous publication [28]. The deposition parameters have been adjusted in order to generate columnar grains with a high concentration of crystalline defects [41]. The film thicknesses were measured by cross-sectional scanning electron microscopy.

The annealing parameters have been selected on the basis of in-situ 4-point probe electrical resistivity measurements, performed on a hot stage in the range 20–350 °C under flowing Ar. Indeed, changes of microstructure during annealing of Pd can be detected by measuring the variation of the resistivity as a function of temperature [42]. These measurements have been carried out with a Linkam LTS 350 heating and freezing stage, connected to an Autolab PGSTAT302N operating in constant-current mode. Currents between 1 and 100 mA have been imposed, without any difference observed in the voltage evolution as a function of temperature. The voltage resolution is equal to 0.3 μV. The temperature was continuously monitored with a TMS 94 temperature controller, and recorded with Linksys 32 software. The distance between each contact point on the rectangular specimen was set equal to the specimen width, and the length over width ratio was larger than 4, therefore avoiding the need for any electrical correction factor [43]. For the annealing cycles on the hot stage, the heating rate was 25 °C/min, and the temperature was maintained for 5 min at 350 °C before the cooling phase. Cooling

was performed by turning off the heating elements and by circulating cooling water through the heating stage. Voltage and temperature were measured in-situ throughout the whole temperature cycle. The temperature coefficient of resistance (TCR) of the Pd films has also been extracted from these measurements.

Focused Ion Beam (FIB) thinning with the lift-out procedure was used for the preparation of cross-section and plan-view TEM thin foils. Both low magnification and High Resolution TEM (HRTEM) were used to characterize the as-deposited, annealed and hydrided Pd films, using a TECNAI G2 (FEG, 200 kV) microscope. Bright Field (BF) and Dark Field (DF) TEM techniques were used to determine quantitative data on the size and aspect ratio of the grains, on the Twin Boundary (TB) density and on the fraction of grains containing TB. Around 100 grains for each film were included in the statistical analysis. In order to ensure that no twins were missed in the BF and DF images, the TEM thin foils were tilted up to 30° along two perpendicular directions. Subsequently, BF images were taken after each 1° tilting. HRTEM was used to investigate microstructural changes at the atomic scale. The dislocation density was measured by counting extra half planes in HRTEM images. For better visualization, a virtual mask was applied on one g-vector in the Fast Fourier Transform (FFT) and then an Inverse Fast Fourier Transform (IFFT) was generated revealing the family of planes related to the selected g. This procedure was performed for all main spots in the FFT patterns. The HRTEM measurements of the dislocation density included grains with different local orientations and grain sizes, since these parameters can affect the local dislocation density developed within individual nanograins.

Background

In this study, the deposition of Pd films – involving internal stress control – has been carried out according to a previously established procedure. Furthermore, the hydriding equilibrium and kinetic behaviours of the Pd films have been interpreted according to models that we developed in previous publications. However, for the sake of understanding, these background elements are briefly presented in this section, and illustrated with the deposition and hydriding experiments performed in this study.

Since the growth-induced internal stress in the films is a function of the argon sputtering pressure p_{Ar} [44], the latter has been adjusted in order to obtain different internal stresses in the Pd films. The objective in this study was to deposit a batch of specimens with zero internal stress, and another batch with a moderate tensile internal stress level. Then, the specimens with zero internal stress will be annealed, so that the thermally-induced stress corresponds to the tensile growth-induced stress level of the other, as-deposited batch. Fig. 2 shows the temporal evolution of the stress*thickness product before and during deposition of the Ti adhesion layer, as well as after Pd deposition, and as a function of Pd thickness for the two batches studied here. After the baseline measurement, the stress in the Ti adhesion layer follows a characteristic bump-like profile, whose interpretation can be found elsewhere [28,45]. Soon after the start of Pd deposition,

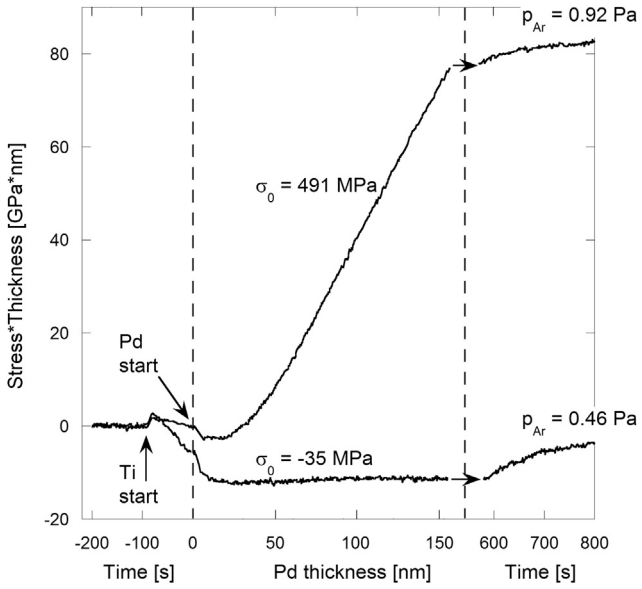

Fig. 2 – Evolution of the stress*thickness product for two different argon sputtering pressures as a function of time before and during Ti layer deposition as well as after Pd deposition, and as a function of Pd thickness during Pd deposition.

the slope of the stress*thickness vs. thickness curve becomes constant. As detailed previously, the sign and magnitude of this slope were both observed to be a function of p_{Ar} [28]. Consequently, one can tune the mean internal stress in the deposit (σ_o) by varying p_{Ar}, as illustrated in Fig. 2.

Regarding hydriding experiments, the bulk hydrogen concentration in the Pd film can be linked to the stress change of Eq. (1) if the deformation is purely elastic [46]:

$$\Delta\sigma = \frac{E_f}{3(1-\nu_f)}\left(\frac{\Delta V}{V}\right) = \frac{E_f}{3(1-\nu_f)}\left(\frac{\Delta v}{\Omega_{Pd}}\right)n \equiv Q\cdot n. \quad (2)$$

In this equation, E_f and ν_f are the Young's modulus and Poisson ratio of the Pd film, respectively, and n is the bulk H/Pd atomic ratio. One can also write $\Delta V/(Vn) = \Delta v/\Omega_{Pd}$, where Ω_{Pd} is the mean atomic volume of a Pd atom and Δv is the characteristic volume change per hydrogen atom. For the sake of clarity, a single proportionality factor Q has been defined in order to collapse all mechano-physical constants of Eq. (2) into a single parameter [46].

Fig. 3a shows two hydriding cycles recorded at similar hydrogen partial pressures (p_{H2}). One of the Pd cantilevers used in these experiments has been cut out of the wafer exhibiting a growth-induced internal stress of 491 MPa. The second one comes from the other deposit with almost zero growth-induced stress, but annealed such as to reach an internal stress of 490 MPa (see next section). As a result, these two specimens have very similar internal stress levels before being subjected to hydrogen cycling. From Fig. 3b, it can be seen that the as-deposited specimen exhibits a much faster hydriding kinetics than the annealed specimen. Indeed, the time needed to reach chemical equilibrium between gaseous hydrogen in the quartz tube and atomic hydrogen inside the Pd film differs by more than one order of magnitude: about

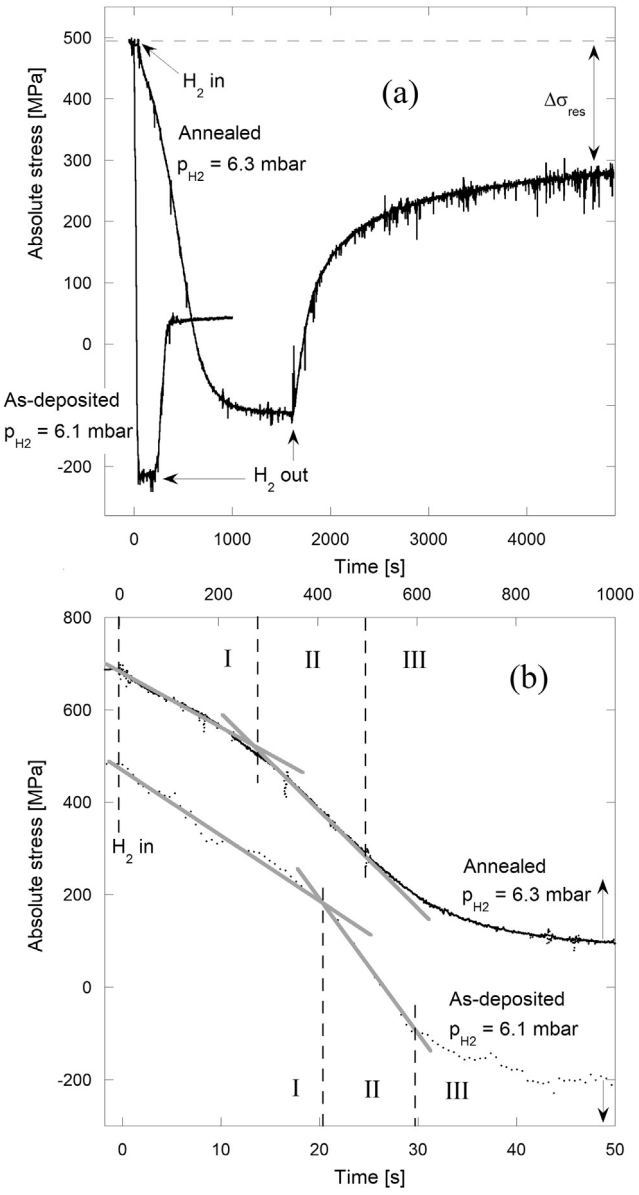

Fig. 3 – (a) Evolution of the hydriding-induced internal stress as a function of time for, respectively, an as-deposited Pd thin film, and a film annealed for 20 min at 300 °C. (b) Zoom on the hydriding kinetics, showing three characteristic regimes for each specimen. An offset of 200 MPa has been applied to the curve corresponding to the annealed specimen for clarity.

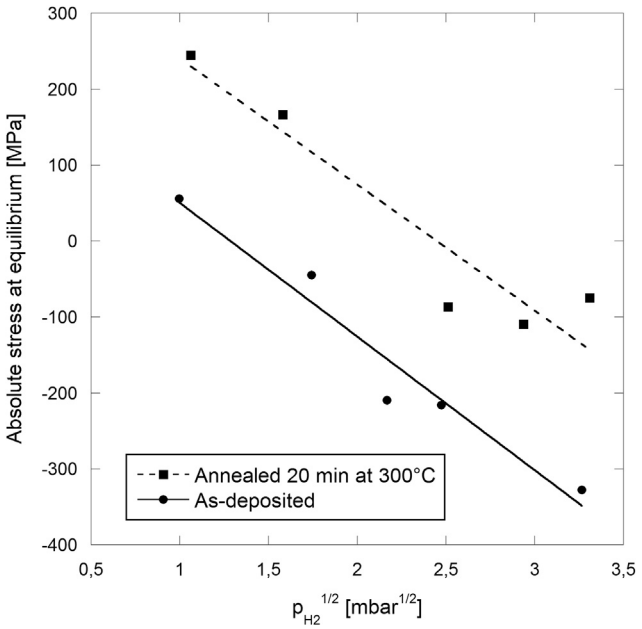

Fig. 4 – Equilibrium internal stress as a function of $p_{H2}^{1/2}$ in the α phase region of the Pd–H system. Two batches with similar internal stresses are compared, one being subjected to hydrogen cycling as-deposited and the other one after annealing 20 min at 300 °C.

100 s for the as-deposited specimen vs. 1000 s for the annealed one. This is, at least qualitatively, the expected behaviour for an annealed thin film undergoing structural recovery of growth-induced defects like grain boundaries, dislocations, twins and vacancies. The dramatic effect on the hydriding kinetics will be discussed more quantitatively in the next section.

In Fig. 4, the internal stress values at equilibrium have been plotted as a function of $(p_{H2})^{1/2}$, thereby validating Sievert's law $K_s = (p_{H2})^{1/2}/n_{eq}$ as already discussed in previous work on as-deposited specimens [28]. However, in order to extract Sievert's constant K_s from the data in Fig. 4, we still need to assess the assumption of a purely elastic deformation in the Pd films during hydriding, which is mandatory to apply Eq. (2) and make a direct quantitative link between the measured stress changes and the hydrogen concentration n. First of all, the internal stress level before hydriding is for all specimens on the order of 500 MPa. This value is well below the tensile yield stress for nanocrystalline Pd, as measured in our group by Colla et al. for Pd films with similar thickness and grain size [47]. Furthermore, the present hydriding experiments have been limited to the relatively low p_{H2} range 1–10 mbar, which ensures to remain in the α phase of the Pd hydride [28,46]. The reported internal stress levels at the hydriding equilibrium are therefore not affected by plasticity effects accompanying the α → β phase transition. Moreover, our internal stress values at equilibrium can also be seen in Fig. 4 to be well below the 1 GPa compressive yield strength of nanocrystalline Pd reported by Youngdahl et al. [48].

The details and relevant constitutive equations for a full quantitative analysis of the hydriding kinetics of the Pd films, as revealed from in-situ stress measurements, have already been presented elsewhere [28,46]. In short, one can start from the observation that two mechanistic steps can be rate-limiting, i.e. H_2 adsorption and dissociative chemisorption on the Pd surface on the one hand (Eq. (3)), and a surface-to-bulk transition followed by interstitial absorption in the Pd lattice on the other hand (Eq. (4)):

$$H_2 + 2s \rightleftharpoons 2H_s, \quad (3)$$

$$H_s + i \rightleftharpoons H_i + s. \quad (4)$$

In the above reactions, s and i represent a free surface adsorption site and an interstitial bulk absorption site, respectively. H_s and H_i represent a surface and bulk site occupied by atomic H, respectively. The temporal derivative of n in, respectively, the adsorption-limited case (Eq. (3)) and the absorption-limited case (Eq. (4)), can then be described analytically as follows [46]:

$$\left(\frac{dn}{dt}\right)_{ad} = \frac{2k'_{ad}K_{ab}^2}{(K_{ab}+n)^2+K_{ab}}\left[p_{H_2}-(K_S n)^2\right], \quad (5)$$

$$\left(\frac{dn}{dt}\right)_{ab} = k'_{ab}\left[(1-n)-\frac{K_S n}{\sqrt{p_{H_2}}}\right], \quad (6)$$

where k'_{ad} and k'_{ab} are the forward rate constants of reactions (3) and (4), respectively. If one defines k''_{ad} and k''_{ab} as the respective backward rate constants of these reactions, then $K_{ad} \equiv k'_{ad}/k''_{ad}$ and $K_{ab} \equiv k'_{ab}/k''_{ab}$ represent the equilibrium constants of reactions (3) and (4), respectively. Since the combination of Eqs. (3) and (4) describes the global hydriding mechanism (from H_2 to H_i), the combination of their equilibrium constants logically results in Sieverts' constant: $K_{ad}(K_{ab})^2 = 1/(K_s)^2$. Delmelle and Proost [46] detail the mathematical developments of these parameters. Here again, the importance of working only in the α phase of the Pd hydride (in order to be able to combine Eq. (2) with Eqs. (5) and (6)) is pointed out. This condition has been respected, as explained above.

With respect to the current experimental hydriding cycles shown in Fig. 3 for both as-deposited and annealed Pd thin film cantilevers, three characteristic kinetic regimes can be distinguished [28,38,46]: directly after hydrogen exposure, a first linear regime is observed (regime I in Fig. 3b), which we have already shown before to be limited by absorption. When the surface coverage reaches a certain level, the heat of adsorption drastically changes, leading to a second linear regime (regime II in Fig. 3b), limited by adsorption. Still later on in the hydriding cycle, the adsorption reaction (3) reaches its equilibrium, but hydrogen atoms can still further be absorbed into the bulk. This marks the beginning of a third, nonlinear kinetic regime (regime III in Fig. 3b), again limited by absorption. This last regime finally ends when absorption equilibrium is reached. More details about this kinetic interpretation can be found in Ref. [46].

Results and discussions

In this section, the annealing cycles undergone by the Pd films have first been optimized through 4-point probe electrical resistivity measurements, in order to identify the onset temperature of defect recovery mechanisms responsible for the relaxation of the internal, growth-induced stress. The annealing and hydriding cycles derived from the in-situ curvature measurement set-up are then interpreted. Next, the kinetic rate expressions described in the previous section are applied to analyze in more details the complete hydriding cycle, and the kinetic model is extended to address the effect of microstructure on the hydriding kinetics. Finally, the latter results are confronted with detailed defect statistics obtained from high-resolution TEM observations.

In-situ study of microstructural changes during annealing

As to the 4-point probe electrical resistivity measurements, the TCR of the films can simply be deduced by combining in-situ voltage and temperature measurements. As the electrical measurement is performed in constant current mode, the ratio U/U_0 between the voltage U at a given temperature and its value U_0 at room temperature is equal to R/R_0, where R is the specimen electrical resistance. This ratio is itself linked to α, the TCR of the film by the following relationship [49]:

$$\frac{R}{R_0} = 1+\alpha(T-T_0). \quad (7)$$

At temperatures close to ambient, this coefficient can be expected to be constant [50], reflecting the classical behaviour of the resistivity of metals at such temperatures, driven by electron-phonon scattering. But according to Matthiessen's rule, two other sources of electron scattering exist, i.e. defects and impurities. Although our Pd films have already been proven to be very pure [28,38,46], one also knows that they can contain a lot of crystalline defects. Their contribution to the resistivity is independent of temperature as long as their concentration is not affected by recovery, recrystallization or grain growth phenomena. If the temperature is high enough for such mechanisms to occur, defect-free channels are created in the lattice, thereby decreasing the TCR. Fig. 5 shows the evolution of the ratio R/R_0 as a function of temperature during a heating cycle performed on a Pd film specimen. The linear behaviour during heating up to 200 °C shows that the film is responding normally, without any apparent change in

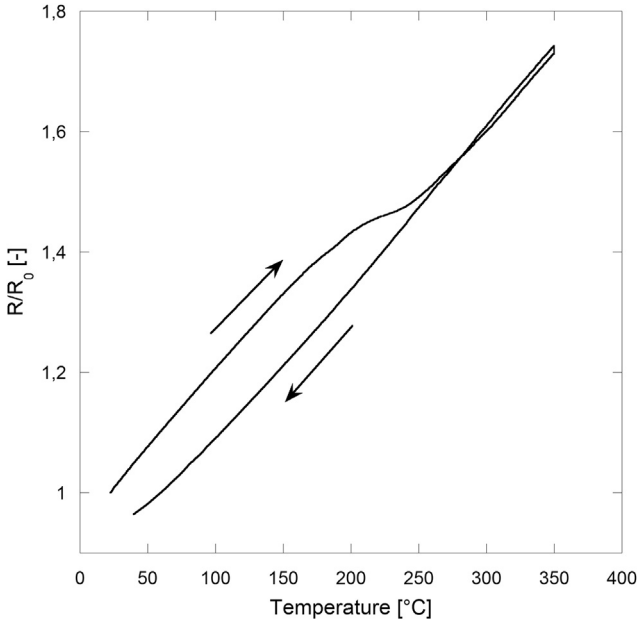

Fig. 5 – Evolution of the ratio R/R_0 as a function of temperature during a heating cycle performed in the range 20–350 °C, with a heating rate of 25 °C/min. The specimen was maintained for 5 min at 350 °C.

defect concentration. The slope of the curve and hence the TCR of the film starts to decrease between 200 and 210 °C, indicating the onset of defect recovery. The temperature at which the Pd films will be maintained during the annealing cycles should thereby be selected above 200 °C. The TCR of the films has been estimated in the interval [20–200 °C] from specimens with different thicknesses in order to compare it to available literature data. The results are shown in Fig. 6, and indicate that the TCR of our nanocrystalline Pd thin films is smaller than the bulk value ($3.77 \cdot 10^{-3}$ K^{-1} [49]), as expected [49,51,52]. One can also clearly see that the TCR increases with increasing film thickness, as previously reported [49,52]. According to Wedler and Alshorachi, the TCR of a thin film can be expressed as a function of its thickness as follows [49]:

$$\alpha = \alpha_0 \left(\frac{1}{1 + K' l_0 / t_f} \right), \tag{8}$$

where α_0 is the TCR of the bulk material having the same defect concentration as the film, l_0 is the mean free path of electrons, and K' is a proportionality factor. A reliable value of l_0 is impossible to obtain, as the electrons in Pd do not behave as a free electron gas. The two last factors thereby cannot be separately estimated. A fit of the TCR with Eq. (8) is performed in Fig. 6, with α_0 and $K' l_0$ as free parameters. This results in $\alpha_0 = (3.1 \pm 0.2) \cdot 10^{-3}$ K^{-1}, a value which is smaller than the bulk value, confirming that the films contain a high concentration of crystalline defects.

As to the internal stress evolution during annealing, Fig. 7 shows that annealing of a Pd cantilever exhibiting an initial growth-induced stress of −35 MPa for 20 min up to 300 °C with an imposed heating rate of 15 °C/min gives rise to a final, thermally-induced stress of 490 MPa. As this is very close to the value of the growth-induced stress of 491 MPa for specimens deposited at 0.92 Pa (cfr. Table 1), these experimental conditions have been chosen for the kinetic analysis performed further on. Note that, because of the rather slow natural cooling of the tube furnace below 200 °C, the internal stress has only been measured at the start of cool-down, with an additional final measurement at the end of the temperature cycle.

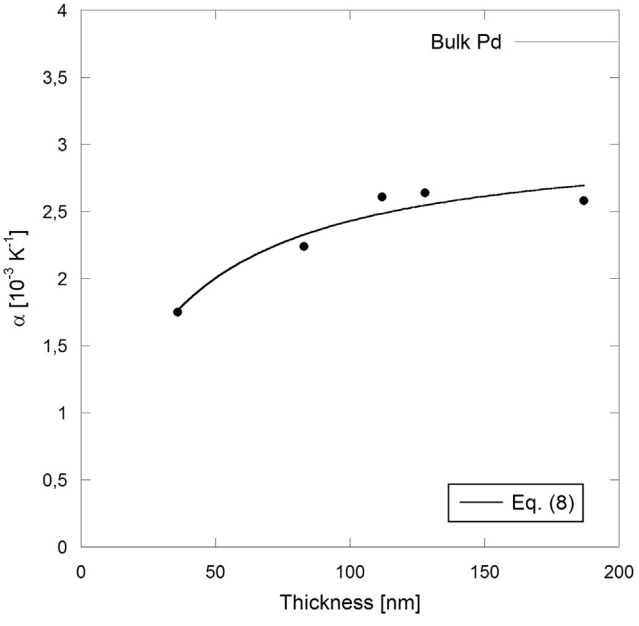

Fig. 6 – TCR of Pd thin films with different thicknesses, fitted with Eq. (8). The value for bulk Pd, taken from Ref. [51], is shown as well.

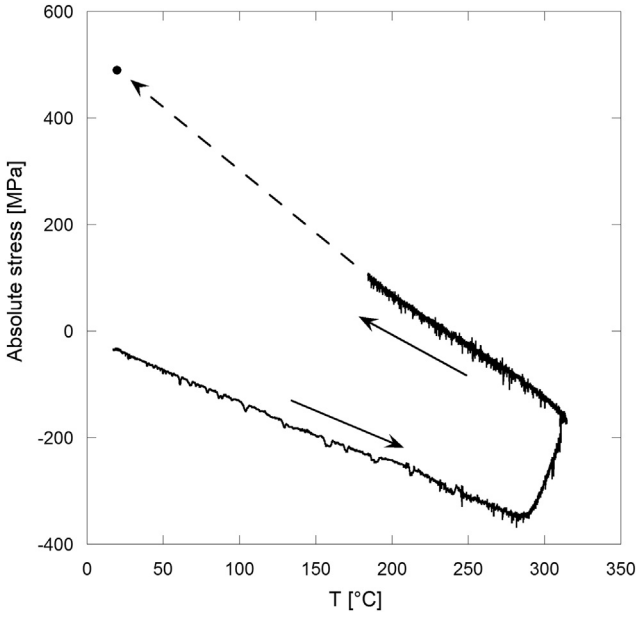

Fig. 7 – Evolution of the internal stress in a Pd thin film as a function of temperature, measured in-situ as the specimen is heated, maintained at 300 °C and cooled down. The last point is the mean of a 500 s measurement performed at room temperature.

During annealing, the biaxial stress change $\Delta\sigma$ undergone by the film can be divided into the following structure-dependent components [31]:

$$\Delta\sigma = \sigma_{th} + \sigma_i + \sigma_e, \tag{9}$$

where σ_i is the intrinsic stress arising from microstructurally-induced volume changes associated with the elimination of growth defects such as grain boundaries, dislocations and point defects [34]. This contribution leads in general to a volume reduction, and can therefore be expected to be tensile. The thermal stress component σ_{th} depends on both the thermal expansion coefficient of the film (α_f) and of its substrate (α_s), according to the following equation [31,53]:

$$\sigma_{th} = \frac{E_f}{1 - \nu_f} (\alpha_S - \alpha_f)(T - T_d), \tag{10}$$

where T is the temperature at which σ_{th} is measured, and T_d is the film deposition temperature. This thermal stress component is expected to be compressive during heating, since $\alpha_s = 0.56 \cdot 10^{-6}$ K^{-1} [54] and $\alpha_f = 11.8 \cdot 10^{-6}$ K^{-1} [55]. Finally, the extrinsic stress σ_e, caused by structural misfits, phase transformations, plastic or creep deformation, chemical reactions, etc. [35], can be neglected here because of the high yield stress of nanocrystalline Pd well above 500 MPa, both in tension [47] and in compression [48]. Let us note that the summation of stress quantities in Eq. (9) is valid here because of the elastic behavior of the film.

Table 1 – Argon plasma pressure p_{Ar}, thickness t_f, average growth-induced stress σ_0 and TEM defect statistics of the Pd films studied in this work. The latter include grain height (perpendicular to the plane of the film) and width (in the plane of the film), aspect ratio (minimum and maximum values), TB and dislocation densities. Data are provided for as-deposited specimens, as well as after annealing and hydriding (α-phase, $p_{H2} = 11$ mbar).

p_{Ar} [Pa]	t_f [nm]	σ_0 [MPa]	Specimen state	Grain height [nm]	Grain width [nm]	Aspect ratio [–]	TB density [1/μm^3]	Dislocation density × 10^{16} [1/m^2]
0.92	157	491	As-dep.	81 ± 6	31 ± 3	1–4	9300 ± 600	8.1 ± 1.4
			After H_2	86 ± 7	30 ± 3	1–4	9500 ± 600	8.8 ± 1.2
0.46	156	−35	As-dep.	102 ± 13	42 ± 6	1–4	8600 ± 500	5.5 ± 1.5
		490	After anneal.	160 ± 5	79 ± 5	1–2	5100 ± 300	3.9 ± 0.9
			After anneal. + H_2	162 ± 6	82 ± 5	1–2	5200 ± 400	5.6 ± 1.3

During the heating phase in Fig. 7, the total stress change is equal to −311 MPa. Knowing that $E_f = 121$ GPa and $\nu_f = 0.39$ [56], one obtains from Eq. (10) that $\sigma_{th} = -602$ MPa. This then results in a value for $\sigma_i = 291$ MPa, both the sign and magnitude of which being indicative for a substantial recovery of growth defects during heating. Although the temperature is then technically maintained at 300 °C, it still slightly increases due to the thermal inertia of the quartz tube. Since the total stress change $\Delta\sigma$ during this plateau is equal to 182 MPa, and the thermal stress component σ_{th} equals −45 MPa, the amount of defect recovery is still important, giving rise to an intrinsic stress contribution σ_i of 227 MPa. Finally, the total stress change during the cooling phase is equal to 654 MPa, very close to the 647 MPa predicted by Eq. (10) for the thermal stress component. This indicates that the defect recovery processes are mainly thermally activated through the heating phase, the amount of tensile intrinsic stress produced during cooling being equal to 7 MPa only.

Hydriding cycle: equilibrium analysis

Let us now analyze the hydriding cycles shown in previous section. Now that the use of Eq. (2) has been validated, we can compute and compare Sieverts' constant K_S for both types specimens shown in Figs. 3 and 4. Taking $\Delta v/\Omega_{Pd} = 0.19$ [57], $E_f = 121$ GPa and $\nu_f = 0.39$ [56], this results in $K_S = 2.4 \pm 0.5$ atm$^{1/2}$ for the as-deposited, and $K_S = 2.2 \pm 0.3$ atm$^{1/2}$ for the annealed batch, respectively. These values, which are statistically equal, indicate that the Pd films contain a high concentration of structural defects as compared to bulk Pd, even after annealing ($K_S \cong 20$ atm$^{1/2}$ for a perfect crystal structure [58]). At the same time, the linear fits performed in Fig. 4 are shifted by about 180 MPa in the compressive direction for the as-deposited specimen. This indicates that, even though the as-deposited and therefore most defective specimens contain more hydrogen, they exhibit a sensitivity to p_{H2} which is similar to the annealed specimens. Consequently, part of the hydrogen absorbed by the Pd films should be located in saturable trapping sites, which are readily filled over the whole p_{H2}-range considered in this study. Hydrogen trapping sites in metals are indeed commonly divided into unsaturable and saturable sites [59,60], part of the latter being irreversible [61,62], i.e. potential wells being too deep to allow hydrogen atoms to escape without external energy. Frappart et al. recently found that the irreversibly trapped hydrogen concentration is constant in the elastic regime [63], which is consistent with our results. This is not the case for the interstitially and reversibly trapped hydrogen, which are both sensitive to the hydrogen partial pressure. Although potential wells corresponding to the reversible traps are deeper than those of the octahedral interstitial sites of the Pd lattice, reversibly trapped hydrogen is still in equilibrium with interstitial hydrogen. As a result, the underlying equilibrium hydrogen concentration n_{eq} involved in the calculation of Sieverts' constant from Fig. 4 will reflect the presence of interstitial and reversibly trapped hydrogen. Consequently, our results indicate that the reversible traps are not significantly modified by annealing, contrary to the irreversible traps like dislocation cores [63]. Our conclusion from Fig. 4 that the as-deposited specimen contains more irreversibly trapped hydrogen than the annealed one would then also imply that the final, residual stress change remaining after the hydriding cycles, corresponding to the equilibrium stress level once hydrogen has been pumped out (cfr. $\Delta\sigma_{res}$ in Fig. 3a), must be higher for the as-deposited specimens as well. From experiments similar to the ones shown in Fig. 3a, this residual stress change $\Delta\sigma_{res}$ was found to be 400 ± 30 MPa for the as-deposited, and 190 ± 10 MPa for the annealed films, respectively, independent of p_{H2} as already inferred from our previous studies on α-PdH [28,46]. The resulting compressive stress difference of 210 ± 30 MPa for the as-deposited specimens thereby confirms our earlier statement that the latter have a higher concentration of irreversible trapping sites. Moreover, this value is also in quantitative agreement with the compressive shift of 180 MPa, observed in Fig. 4 at the hydriding equilibrium.

Hydriding cycle: kinetic analysis

One can find in Figs. 8 and 9 plots of the slopes of the first and second kinetic regimes – as introduced in previous section – with respect to p_{H2}, which have been fitted according to Eq. (6) or (5). Since our previous work already indicated that k'_{ab} shows a linear dependency with p_{H2} [28], this has also been taken into account in Eq. (6) and hence in the fits shown in Fig. 8. Let us firstly examine Figs. 8 and 9 from a qualitative point of view. The fits indicate that the first and second linear kinetic regimes are indeed respectively limited by absorption and adsorption, as addressed before with similar specimens and in similar conditions [28,46]. From Fig. 8, it is also clear that the microstructure of the Pd films has a very important effect on their hydriding velocity, the latter being significantly slowed down for the annealed specimen in the first, absorption-limited regime. Therefore, at least one of the kinetic parameters in Eq. (6) must be strongly affected by the

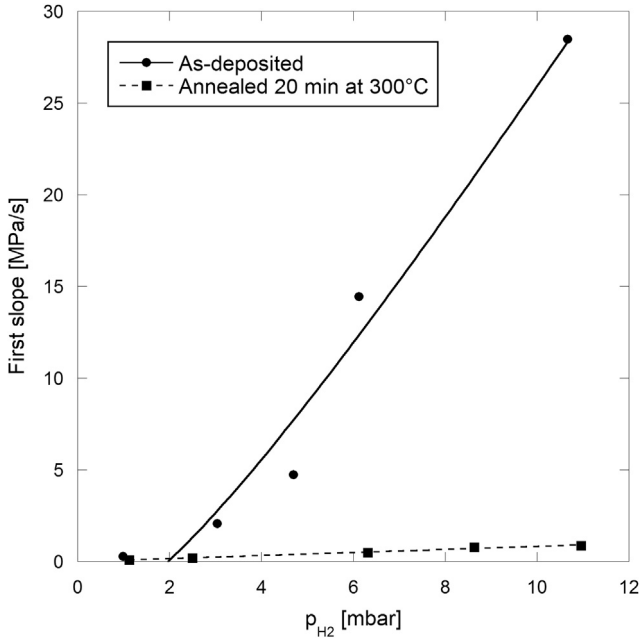

Fig. 8 – Slope of the first linear kinetic regime as a function of p_{H2}, fitted with Eq. (6) and assuming a linear p_{H2}-dependence of k'_{ab} according to Ref. [28].

microstructure. As Sievert's constant K_s has been shown above to be statistically equal for the two types of specimens, the only possible parameter that is strongly microstructure dependent should be k'_{ab}. Similarly, Fig. 9 also shows an important decrease of the hydriding velocity of the annealed Pd specimens in the second, adsorption-limited regime. Therefore, as opposed to internal stress which we have shown previously to have no effect on the rate constants of the adsorption-limited regime [28], microstructure does affect both the absorption- and adsorption-related kinetic parameters. With respect to the latter, one can expect from Eq. (5) that it is again k'_{ab} that is the main microstructure-dependent kinetic parameter. Indeed, since the concentration of reversible traps present on the surface and in the bulk is not significantly altered upon annealing, as discussed in the previous section, the equilibrium parameter K_{ab} should be very similar for the as-deposited and annealed specimens.

Let us now quantitatively study the rate constants of the hydriding mechanism, starting with k'_{ab} in the first kinetic regime. Since Eq. (6) is a simple Cauchy problem, the temporal evolution of n can be easily deduced and fitted to the data of the first kinetic regime at every p_{H2} value. And since K_s is known from our thermodynamical data, this provides a direct access to k'_{ab} (see Ref. [46] for more details). Fig. 10 shows the values of k'_{ab} in the first kinetic regime. A decrease by a factor 30 ± 4 is observed between the k'_{ab} values of the annealed specimens as compared to the as-deposited ones. This factor can be further unraveled by detailing the slopes of the linear fits shown in Fig. 10 as follows [28]:

$$\begin{cases} \dfrac{k'_{ab,adep}}{p_{H_2}} = A'_{ab,adep} \cdot \exp\left(\dfrac{-\Delta H^{0\ddagger}_{ab,adep}}{RT}\right) \\ \dfrac{k'_{ab,ann}}{p_{H_2}} = A'_{ab,ann} \cdot \exp\left(\dfrac{-\Delta H^{0\ddagger}_{ab,ann}}{RT}\right) \end{cases}, \tag{11}$$

where the subscripts $_{adep}$ and $_{ann}$ refer to the as-deposited and annealed specimens, respectively. The high ratio $k'_{ab,adep}/k'_{ab,ann} = 30 \pm 4$ might then result from an effect of microstructure on the pre-exponential factor A'_{ab} and/or an effect of microstructure on the activation enthalpy for hydrogen absorption $\Delta H^{0\ddagger}_{ab}$. To give an idea of this effect, if one

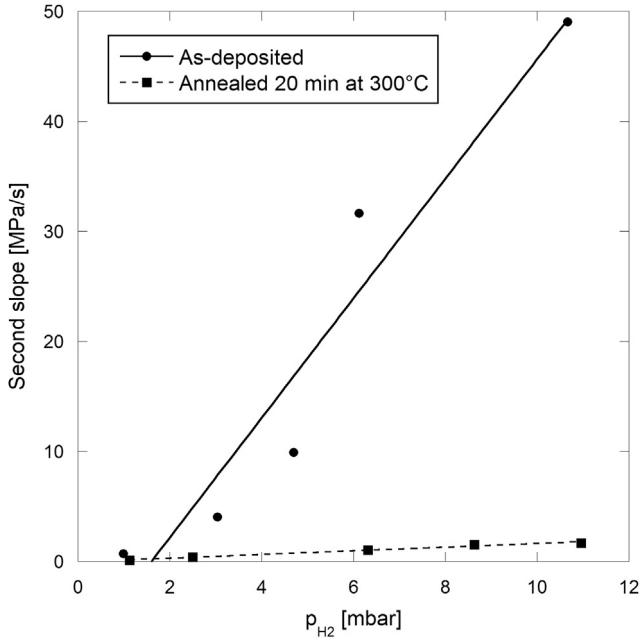

Fig. 9 – Slope of the second linear kinetic regime as a function of p_{H2}, fitted with Eq. (5).

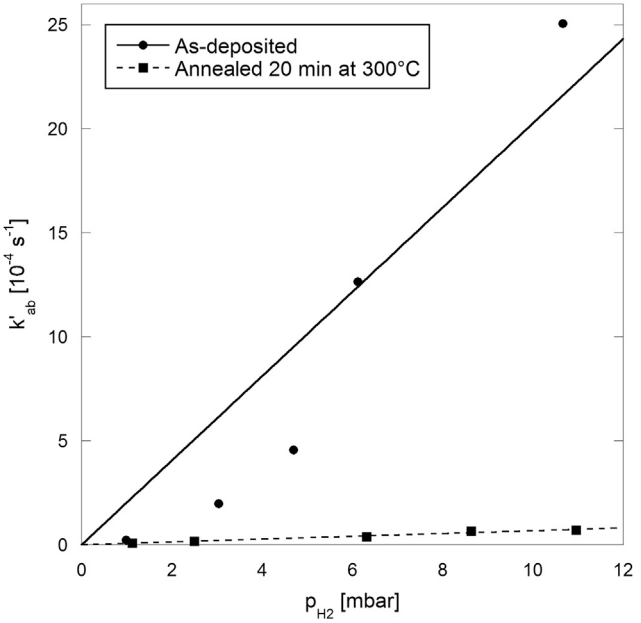

Fig. 10 – Rate constant for hydrogen absorption as a function of p_{H2}. Linear fits are shown for each set of specimens.

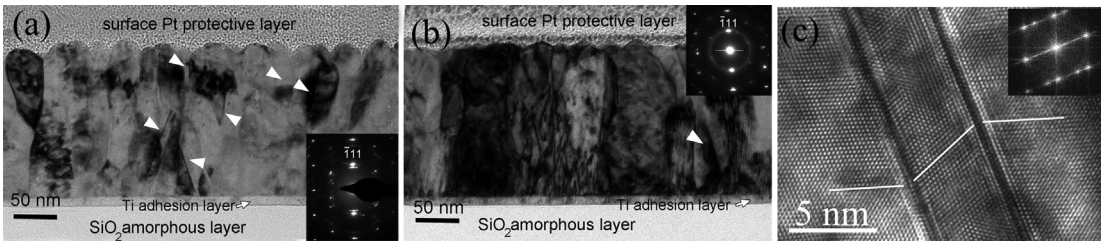

Fig. 11 – BF micrographs of cross-sectional FIB foils of (a) as deposited Pd film ($p_{Ar} = 0.92$ Pa, $\sigma_0 = 491$ MPa) and (b) after annealing at 300 °C for 20 min ($p_{Ar} = 0.46$ Pa, $\sigma_0 = 490$ MPa). Growth twins are indicated by white arrows. Corresponding selected area diffraction patterns are presented in each figure. (c) HRTEM image of growth twin boundaries in the as-deposited film.

considers that $\Delta H_{ab}^{0\ddagger}$ is the main microstructure-affected parameter, one gets $\Delta H_{ab,ann}^{0\ddagger} - \Delta H_{ab,adep}^{0\ddagger} \cong \ln 30\ RT = 8.5$ kJ/mol, i.e. on the order of 10% of the energy of regular surface sites (around 100 kJ/mol [64,65]). However, the quantitative decoupling of the respective effects of A'_{ab} and $\Delta H_{ab}^{0\ddagger}$ on k'_{ab} requires the present kinetic study to be carried out at different temperatures. Further modifications of our experimental setup have been planned for this purpose.

Finally, as to the rate constant for hydrogen adsorption k'_{ad}, its value can be extracted from Eq. (5) by using a 4th order Runge-Kutta algorithm to simulate the evolution of n in the second linear kinetic regime [28,46]. In agreement with the qualitative trend already shown in Fig. 9, k'_{ad} is higher by a factor 40 for the as-deposited batch ($(260 \pm 50)\cdot 10^{16}$ mbar^{-1} s^{-1}) than for the annealed one ($(7 \pm 2)\cdot 10^{16}$ mbar^{-1} s^{-1}). Since it is well-known that there is no activation barrier for hydrogen adsorption onto clean Pd surfaces [66], this would imply that it is the jump frequency for hydrogen adsorption that is increased, presumably by the presence of additional surface defects generated by the thin film deposition process.

Evolution of crystalline defects during annealing and room-temperature hydriding

The main goal of this section is to address in more details the exact nature of the microstructural defects that are responsible for the increase in activation energy for hydrogen absorption upon annealing. In this respect, Fig. 11 shows cross-sectional BF-TEM images obtained on as-deposited (a) and annealed (b) Pd films, respectively. Fig. 11a clearly reveals the columnar, nano-crystalline morphology of the films, with at least two grains along the film thickness. The selected-area diffraction pattern (SADP) shown in the lower right part of Fig. 11a reveals that the film exhibits a strong <111> crystallographic texture. Some growth twins, indicated by white arrows, can be observed as well. The HRTEM image of Fig. 11c shows an example of a Σ3 {111} twin boundary (TB) observed in the as-deposited films. Fig. 11b shows that both the morphological and crystallographic texture have been preserved during the annealing cycle. At the same time, a clear increase in grain size and aspect ratio can be seen, together with a decrease in the number of growth twins. The results of a detailed statistical analysis of grain size, TB density and dislocation density are summarised in Table 1 for the as-deposited, annealed and hydrided Pd specimens. First of all, it is clear that both the height and width of the grains are affected by grain growth during annealing, their average values increasing by a factor 1.6 and 1.9, respectively. As a result, the fraction of grain boundaries is significantly decreased after annealing, both in the film plane as in the thickness direction. The higher grain boundary density in the as-deposited film is therefore believed to contribute to its improved hydriding kinetics by offering low-energy trapping sites for hydrogen – then affecting $\Delta H_{ab}^{0\ddagger}$ – and/or by affecting the jump frequency for surface-to-bulk transition A'_{ab}.

Fig. 12 shows the evolution of the dislocation density measured using HRTEM in as-deposited, annealed and hydrided specimens. The relative scatter in these measurements is caused by local differences in the size of the individual nanocrystalline grains used for the HRTEM measurements. The dislocation density is seen to decrease by almost 30% after annealing (A → B). The higher dislocation density in the as-deposited film thereby also contributes to the faster hydriding kinetics [14,15] and increased equilibrium H-concentration [1,9]. At the same time, the twin boundary density is decreased by 40%, which also implies that twins

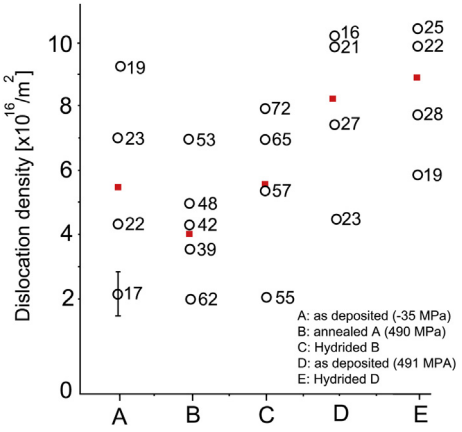

Fig. 12 – Evolution of the average dislocation density (red solid squares) in the Pd films during annealing and hydriding. The numbers aside the unfilled circles indicate the corresponding grain size (in nm) of individual measurements. (For interpretation of the references to colour in this figure legend, the reader is referred to the web version of this article.)

contribute to the acceleration of the hydriding kinetics [26] in the as-deposited specimens. It is worth mentioning here that growth-induced twin boundaries were observed to be closely connected to grain boundaries. Thus, the decrease in TB density after annealing can be attributed to the shrinking or complete disappearance of grains containing twins, as previously observed by Wang et al. [67]. On the other hand, while grain boundaries and lattice dislocations can be expected to generate saturable, irreversible hydrogen traps, twins are unlikely to generate such traps in Pd.

To summarize, an important enhancement of the hydriding kinetics is linked here to the introduction of a heterogeneous collection of defects – notably an heterogeneity of irreversible trapping sites – in the material. Indeed, the rate constant for hydrogen absorption k'_{ab} turns out to be significantly affected. To which extent this effect is due to a change of the jump frequency for surface-to-bulk transition and/or of the activation enthalpy for hydrogen absorption remains an open question. The fact that the rate constant for hydrogen adsorption k'_{ad} is significantly affected as well suggests that the annealing process also affected the surface defect concentrations. Further surface characterization efforts are needed in order to support this result. Finally, one can notice from Table 1 that hydriding within the α phase does not significantly modify the defect concentrations, apart from the dislocation density which clearly increases after hydriding, especially in the annealed specimen. An experimental study on this specific subject is currently being conducted.

Conclusions

In this study, the use of a unique high resolution in-situ experimental setup allowed adjusting the annealing conditions of Pd thin films in order to obtain specimens with similar internal stresses but significantly different microstructures. The analysis of hydriding-induced internal stress changes at equilibrium and after pumping down brought the following conclusions: the concentration of reversible traps in the palladium lattice is not significantly affected by annealing, while the concentration of saturable, irreversible traps is decreased. The use of a self-consistent kinetic model then allowed identifying the rate-limiting steps involved in the hydriding mechanism and calculating the rate constants for hydrogen adsorption and absorption in the Pd films. An important effect of microstructure on both the adsorption and absorption kinetics has been observed. A full quantitative kinetic analysis at room temperature confirmed these tendencies, showing the important potential of defect engineering on both the rate constants for dissociative adsorption – k'_{ad} increase by a factor 40 – and surface-to-bulk transition – k'_{ab} increase by a factor 30. A complementary TEM analysis revealed a decreasing effect of annealing on the densities of grain boundaries – grain height decrease by 36%, grain width decrease by 47% –, dislocations – dislocation density decrease by 30% – and twins – TB density decrease by 40% –, supporting our results obtained on both the microstructure-dependent hydriding kinetics and thermodynamics. Although twin boundaries are not expected to generate irreversible traps, it clearly appears that lattice dislocations and grain boundaries are sources of irreversible traps in our Pd thin films. In our opinion, the interplay between stress, microstructure and hydriding kinetics should be a primary concern in design and optimization of engineering applications in hydrogen storage materials, hydrogen separation membranes or hydrogen detection.

Acknowledgements

This work was funded by the Belgian National Science Foundation through a FRIA doctoral fellowship (grant number FC 83810). The authors also acknowledge the support of the Belgian Interuniversity Attraction Poles (IAP) programme (7/21).

REFERENCES

[1] Pundt A, Kirchheim R. Hydrogen in metals: microstructural aspects. Annu Rev Mater Res 2006;36:555.
[2] Weissmüller J, Lemier C. Lattice constants of solid solution microstructures: the case of nanocrystalline Pd-H. Phys Rev Lett 1999;82:213.
[3] Mütschele T, Kirchheim R. Segregation and diffusion of hydrogen in grain boundaries of palladium. Scr Metall 1987;21:135.
[4] Mütschele T, Kirchheim R. Hydrogen as a probe for the average thickness of a grain boundary. Scr Metall 1987;21:1101.
[5] Yao J, Cahoon J. Experimental studies of grain boundary diffusion of hydrogen in metals. Acta Metall Mater 1991;39:119.
[6] Janssen S, Natter H, Hempelmann R, Striffler T, Stuhr U, Wipf H, et al. Hydrogen diffusion in nanocrystalline Pd by means of quasielastic neutron scattering. Nano Mater 1997;9:579.
[7] Kirchheim R. Hydrogen solubility and diffusivity in defective and amorphous metals. Prog Mater Sci 1988;32:261.
[8] Oudriss A, Creus J, Bouhattate J, Savall C, Peraudeau B, Feaugas X. The diffusion and trapping of hydrogen along the grain boundaries in polycrystalline nickel. Scr Mater 2012;66:37.
[9] Myers SM, Baskes MI, Birnbaum HK, Corbett JW, DeLeo GG, Estreicher SK, et al. Hydrogen interactions with defects in crystalline solids. Rev Mod Phys 1992;64:559.
[10] Pivak Y, Schreuders H, Slaman M, Griessen R, Dam B. Thermodynamics, stress release and hysteresis behavior in highly adhesive Pd-H films. Int J Hydrogen Energy 2011;36:4056.
[11] Maxelon M, Pundt A, Pyckhout-Hintzen W, Barker J, Kirchheim R. Interaction of hydrogen and deuterium with dislocations in palladium as observed by small angle neutron scattering. Acta Mater 2001;49:2625.
[12] Maxelon M, Pundt A, Pyckhout-Hintzen W, Kirchheim R. Small angle neutron scattering of hydrogen segregation at dislocations in palladium. Scr Mater 2001;44:817.
[13] Kirchheim R. Interaction of hydrogen with dislocations in palladium-I. Activity and diffusivity and their phenomenological interpretation. Acta Metall 1981;29:835.
[14] Tien J, Thompson A, Bernstein I, Richards R. Hydrogen transport by dislocations. Metall Mater Trans A 1976;7:821.
[15] Mommer N, Hirscher M, Cuevas F, Kronmüller H. Influence of the microstructure on the desorption kinetics of single- and multiphase LaNiFe alloys. J Alloy Compd 1998;266:255.

[16] Fukai YJ. Formation of superabundant vacancies in M-H alloys and some of its consequences: a review. Alloy Compd 2003;356–357:263.
[17] Fukai Y, Ōkuma N. Formation of superabundant vacancies in Pd hydride under high hydrogen pressures. Phys Rev Lett 1994;73:1640.
[18] Isaeva LE, Bazhanov DI, Isaev EI, Eremeev SV, Kulkova SE, Abrikosov IA. Dynamic stability of palladium hydride: An ab initio study. Int J Hydrogen Energy 2011;36:1254.
[19] He JH, Dechiaro LF, Knies DL, Hubler GK, Grabowski KS, Moser AE, et al. Stability of a hydrogen molecule in a vacancy of palladium hydrides. Int J Hydrogen Energy 2012;37:12351.
[20] Carr NZ, McLellan RB. The thermodynamic and kinetic behavior of metal-vacancy-hydrogen systems. Acta Mater 2004;52:3273.
[21] Singh S, Eijt SWH. Hydrogen vacancies facilitate hydrogen transport kinetics in sodium hydride nanocrystallites. Phys Rev B 2008;78:224110.
[22] Borgschulte A, Bielmann M, Züttel A, Barkhordarian G, Dornheim M, Bormann R. Hydrogen dissociation on oxide covered MgH_2 by catalytically active vacancies. Appl Surf Sci 2008;254:2377.
[23] Mine Y, Tachibana K, Horita Z. Grain-boundary diffusion and precipitate trapping of hydrogen in ultrafine-grained austenitic stainless steels processed by high-pressure torsion. Mater Sci Eng A 2011;528:8100.
[24] Koyama M, Akiyama E, Sawaguchi T, Raabe D, Tsuzaki K. Hydrogen-induced cracking at grain and twin boundaries in an Fe-Mn-C austenitic steel. Scr Mater 2012;66:459.
[25] So KH, Kim JS, Chun YS, Park KT, Lee YK, Lee CS. Hydrogen delayed fracture properties and internal hydrogen behavior of a Fe–18Mn–1.5Al–0.6C TWIP steel. ISIJ Int 2009;49:1952.
[26] Danaie M, Tao S, Kalisvaart P, Mitlin D. Analysis of deformation twins and the partially dehydrogenated microstructure in nanocrystalline magnesium hydride (MgH_2) powder. Acta Mater 2010;58:3162.
[27] Amin-Ahmadi B, Idrissi H, Delmelle R, Pardoen T, Proost J, Schryvers D. High resolution transmission electron microscopy characterization of fcc→9R transformation in nanocrystalline palladium films due to hydriding. Appl Phys Lett 2013;102:071911.
[28] Delmelle R, Michotte S, Sinnaeve M, Proost J. Effect of internal stress on the hydriding kinetics of nanocrystalline Pd thin films. Acta Mater 2013;61:2320.
[29] Wicke E, Brodowsky H. Hydrogen in palladium and palladium alloys. In: Alefeld G, Voelkl J, editors. Hydrogen in metals, vol. 2. Berlin: Springer Verlag; 1978.
[30] Lewis FA. The palladium hydrogen system. London: Academic Press; 1967.
[31] Daniel R, Holec D, Bartosik M, Keckes J, Mitterer C. Size effect of thermal expansion and thermal/intrinsic stresses in nanostructured thin films: experiment and model. Acta Mater 2011;59:6631.
[32] Kumar D, Gupta A. Evolution of structural and magnetic properties of sputtered nanocrystalline Co thin films with thermal annealing. J Magn Magn Mater 2007;308:318.
[33] Köstenbauer H, Fontalvo GA, Kapp M, Keckes J, Mitterer C. Annealing of intrinsic stresses in sputtered TiN films: the role of thickness-dependent gradients of point defect density. Surf Coat Technol 2007;201:4777.
[34] Karlsson L, Hörling A, Johansson M, Hultman L, Ramanath G. The influence of thermal annealing on residual stresses and mechanical properties of arc-evaporated TiC_xN_{1-x} ($x = 0$, 0.15 and 0.45) thin films. Acta Mater 2002;50:5103.
[35] Daniel R, Martinschitz K, Keckes J, Mitterer C. The origin of stresses in magnetron-sputtered thin films with zone T structures. Acta Mater 2010;58:2621.
[36] Xu H, Heinrich H, Wiezorek JM. Microstructural changes during annealing of FePd-based thin films. Intermetallics 2003;11:963.
[37] Miller DC, Herrmann CF, Maier HJ, George SM, Stoldt CR, Gall K. Intrinsic stress development and microstructure evolution of Au/Cr/Si multilayer thin films subject to annealing. Scr Mater 2005;52:873.
[38] Delmelle R, Bamba G, Proost J. In-situ monitoring of hydride formation in Pd thin film systems. Int J Hydrogen Energy 2010;35:9888.
[39] Van Overmeere Q, Vanhumbeeck JF, Proost J. On the use of a multiple beam optical sensor for in situ curvature monitoring in liquids. Rev Sci Instrum 2010;81:045106.
[40] Proost J, Spaepen F. Evolution of the growth stress, stiffness, and microstructure of alumina thin films during vapor deposition. J Appl Phys 2002;91:204.
[41] Thornton JA. Influence of apparatus geometry and deposition conditions on the structure and topography of thick sputtered coatings. J Vac Sci Technol 1974;11:666.
[42] Ichinohe T, Masaki S, Uchida K, Nozaki S, Morisaki H. Fabrication of nanostructured palladium-doped SiO_2 films with variable temperature coefficient of resistivity. Thin Solid Films 2004;466:27.
[43] Smits FM. Measurement of sheet resistivities with the four-point probe. Bell Sys Tech J 1958;37:711.
[44] Thornton JA, Tabock J, Hoffman DW. Internal stresses in metallic films deposited by cylindrical magnetron sputtering. Thin Solid Films 1979;64:111.
[45] Floro JA, Hearne SJ, Hunter JA, Kotula P, Chason E, Seel SC, et al. The dynamic competition between stress generation and relaxation mechanisms during coalescence of Volmer-Weber thin films. J Appl Phys 2001;89:4886.
[46] Delmelle R, Proost J. An in situ study of the hydriding kinetics of Pd thin films. Phys Chem Chem Phys 2011;13:11412.
[47] Colla MS, Wang B, Idrissi H, Schyvers D, Raskin JP, Pardoen T. High strength-ductility of thin nanocrystalline palladium films with nanoscale twins: on-chip testing and grain aggregate model. Acta Mater 2012;60:1795.
[48] Youngdahl CJ, Sanders PG, Eastman JA, Weertman JR. Compressive yield strengths of nanocrystalline Cu and Pd. Scr Mater 1997;37:809.
[49] Wedler G, Alshorachi G. The influence of thickness on the resistivity, the temperature coefficient of resistivity and the thermoelectric power of evaporated palladium films at 77 K and 273 K. Thin Solid Films 1980;74:1.
[50] De Vries JWC. Temperature and thickness dependence of the resistivity of thin polycrystalline aluminium, cobalt, nickel, palladium, silver and gold films. Thin Solid Films 1988;167:25.
[51] Tripodi P, Armanet N, Asarisi V, Avveduto A, Marmigi A, Vinko JD, et al. The effect of hydrogenation/dehydrogenation cycles on palladium physical properties. Phys Lett A 2009;373:3101.
[52] Shivaprasad SM, Angadi MA. Temperature coefficient of resistance of thin palladium films. J Phys D Appl Phys 1980;13:L171.
[53] Hanabusa T, Kusaka K, Sakata O. Residual stress and thermal stress observation in thin copper films. Thin Solid Films 2004;459:245.
[54] Tada H, Kumpel AE, Lathrop RE, Slanina JB, Nieva P, Zavracky P, et al. Thermal expansion coefficient of polycrystalline silicon and silicon dioxide thin films at high temperatures. J Appl Phys 2000;87:4189.
[55] Kuru Y, Wohlschlögel M, Welzel U, Mittemeijer E. Coefficients of thermal expansion of thin metal films investigated by non-ambient X-ray diffraction stress analysis. Surf Coat Technol 2008;202:2306.

[56] Smithells CJ. Metals reference book. 8th ed. London: Butterworths; 2004.
[57] Peisl H. Lattice strains due to hydrogen in metals. In: Alefeld G, Voelkl J, editors. Hydrogen in metals, vol. 1. Berlin: Springer Verlag; 1978.
[58] Bucur RV. Effect of trapping on the solubility and diffusivity of hydrogen in palladium (α-phase). J Mater Sci 1987;22:3402.
[59] Krom A, Bakker A. Hydrogen trapping models in steel. Metall Mater Trans B 2000;31:1475.
[60] Young GA, Scully J. The diffusion and trapping of hydrogen in high purity aluminum. Acta Mater 1998;46:6337.
[61] Cao Y, Li H, Szpunar J, Shmayda W. Modeling of hydrogen trapping in the deformed Pd and $Pd_{77}Ag_{23}$ alloy. Mater Sci Eng A 2004;379:173.
[62] Frappart S, Feaugas X, Creus J, Thebault F, Delattre L, Marchebois H. Study of the hydrogen diffusion and segregation into FeCMo martensitic HSLA steel using electrochemical permeation test. J Phys Chem Sol 2010;71:1467.
[63] Frappart S, Feaugas X, Creus J, Thebault F, Delattre L, Marchebois H. Hydrogen solubility, diffusivity and trapping in a tempered Fe-C-Cr martensitic steel under various mechanical stress states. Mater Sci Eng A 2012;534:384.
[64] Jewell JJ, Davis BH. Review of absorption and adsorption in the hydrogen-palladium system. Appl Catal A 2006;310:1.
[65] Johansson M, Skúlason E, Nielsen G, Murphy S, Nielsen RM, Chorkendorff I. Hydrogen adsorption on palladium and palladium hydride at 1 bar. Surf Sci 2010;604:718.
[66] Ward TL, Dao T. Model of hydrogen permeation behavior in palladium membranes. J Membr Sci 1999;153:211.
[67] Wang B, Idrissi H, Shi H, Colla M-S, Michotte S, Raskin J-P, et al. Texture-dependent twin formation in nanocrystalline thin Pd films. Scr Mater 2012;66:866.